Concrete Science and Engineering, Vol. 1, September 1999, pp 173-174

On interface property characterization and performance of fiber-reinforced cementitious composites

Z. Lin[1], T. Kanda[2] and V. C. Li[1]
(1) Advanced Civil Engineering Materials Research Laboratory, Department of Civil and Environmental Engineering, University of Michigan, Ann Arbor, MI 48109-2125, USA
(2) Kajima Technical Research Institute, 2-19-1 Tobitakyu, Chofu-shi, Tokyo 182, Japan

ABSTRACT

It has been well recognized that fiber/matrix interface properties have significant effects on the performance of a fiber-reinforced cement composite, including its fracture toughness, tensile and flexural strength and ductility. Proper characterization of the interface properties via micromechanics models can lead to effective tools for designing high performance and cost-effective cement-based materials. In this paper, a micromechanics model is developed to characterize the interface properties at single fiber pullout level. In the model, interfacial fracture toughness, frictional bond strength and post-debonding slip-hardening coefficient are explicitly accounted for. Fiber rupture and fiber strength reduction due to inclined fiber pullout are also considered. The complete composite bridging stress versus crack opening curve (σ_B - δ relation) is derived analytically. Implications of the present model on various composite properties, including composite tensile strength, fracture energy and complementary energy (a measure of ductility), are discussed along with an example of PVA fiber reinforced cement composites.

1. INTRODUCTION

Introduction of fibers in a cement-based brittle matrix can significantly increase the failure strain and fracture toughness of the composite by orders of magnitude [1-4]. In order to achieve high performance and cost-effectiveness of such composites, quantitative materials design tools are needed. Micromechanics models have been proven to be very effective in high performance and cost-effective cement-based composites development [5-7]. A generation of super-ductile short-fiber cement composites so-called Engineered Cementitious Composites (ECC) have been developed and start to gain momentum in real-world applications [8-10]. Presented in this paper is a generic micromechanics model that can be used for almost all the fiber types, including steel fibers and synthetic (polymeric) fibers with both hydrophobic and hydrophilic nature. The current model extends the work by Maalej *et al.* [3] to include chemical bonding and slip-dependent interfacial properties. It provides not only a more realistic representation of fiber-matrix interfacial behaviors in many cases but also significantly broadens the range of viable fiber types in achieving both high performance and cost-effectiveness, especially for those fibers with strong chemical bond to cement matrix such as Poly-Vinyl-Alchohol (PVA) fiber, which will be investigated in detail. Fig. 1 shows the scope of the present work within the performance driven design approach (PDDA) [11].

The remainder of this paper is organized as follows. A theoretical single fiber debonding and pullout model is first presented with three most important, physically meaningful parameters: (1) Chemical bond strength quantified by interfacial fracture toughness, (2) constant frictional bond strength for small sliding and (3) slip-hardening coefficient that characterizes the increasing effective frictional bond during large sliding (pullout) stage [7, 12]. Then, a composite bridging stress versus crack opening (σ_B - δ) relation is derived in closed-form based on the single fiber pullout model and random fiber distribution assumption. As a fundamental material

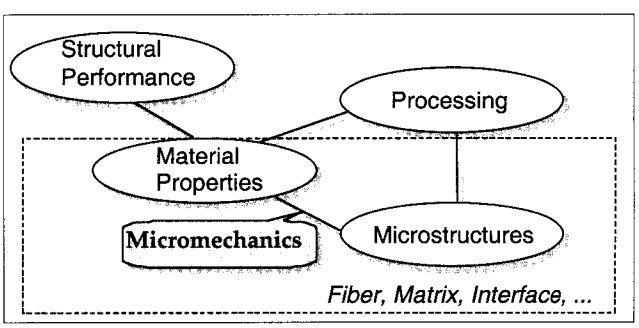

Fig. 1 – Scope of the present research within the Performance Driven Design Approach.

property, the σ_B - δ relation has been well recognized as a crucial link between composite constituents and overall composite properties. Most direct and important implications of this model including tensile strength and ductility are presented in the following section along with an example of PVA fiber-cement composite. Conclusions drawn from the current research are made in the end.

2. INTERFACE CHARACTERIZATION

A commonly-used technique to investigate fiber-matrix interfacial behaviors is single fiber pullout. Fig. 2 shows schematically the set-up for a typical single fiber pullout test. The specimens are fabricated according to the technique for microfibers described in [13] in order to ensure accurate alignment. The tensile load on the fiber is measured with a miniature load cell of 1-Newton capacity. Fig. 3 is a typical pullout curve for a PVA fiber of 14.8 μm diameter. The fiber embedment length L_e is chosen in such a way that fiber rupture is avoided during the whole process and both debonding and frictional pullout behaviors can be completely captured.

As can be seen from Fig. 3, there are three stages associated with the load-displacement curve: initial elastic stretching of the fiber free length (the portion not embedded), followed by debonding stage, which is simulated in the present model by a mode-II tunneling crack advance with non-zero crack-tip fracture toughness. The debonding stage continues until reaching the maximum load and a distinct load drop occurs. This load drop is an indication of chemical bonding because it would not appear if the interface is frictionally bonded only. Physically, the load drop represents the transition from both chemical bond and frictional bond controlled debonding stage to the pullout stage with frictional bond only. After complete debonding of the interface, chemical bond does not exist but frictional bond could effectively increase due to fabrillation of fiber surface sliding against surrounding matrix. A concave upward portion of the curve indicates this so-called slip-hardening behavior, which has been investigated elsewhere [7, 12].

A theoretical single fiber debonding and pullout model is derived, based on simple stress analysis and energy balance principle (see Appendix -A). The main assumptions made in this model are:

(1) Fibers are of high aspect ratio (> 100) so that the end effect on the total debonding load is negligible. This assumption is generally satisfied for most available fibers, and it greatly simplifies the analysis without losing accuracy.

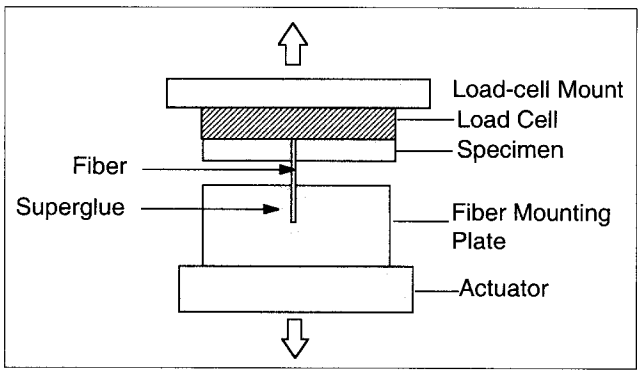

Fig. 2 – Schematic of a single fiber pullout test set-up.

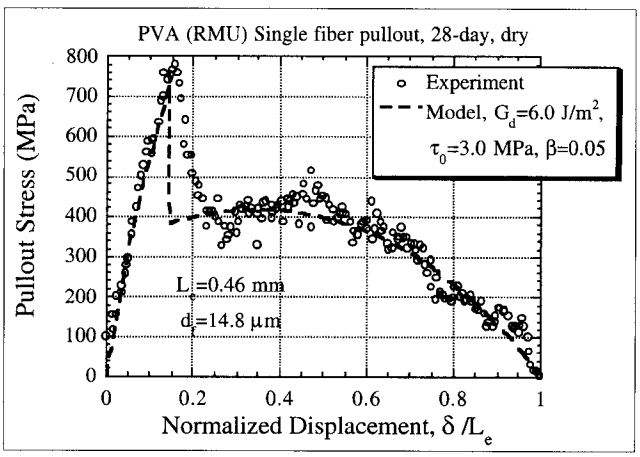

Fig. 3 – Single fiber pullout curve of a PVA fiber: test result vs. model prediction

(2) During the debonding stage, the slip-dependent effect is negligible since relative slippage between the fiber and the matrix in the debonded portion is small. Hence, the frictional stress within the debonded zone remains at a constant τ_0.

(3) Poisson's effect is negligible. For flexible fiber/cement systems, Poisson's effect is usually diminished due to inevitable slight misalignment and surface roughness of the fiber (no alignment at all in a random, short fiber composite) [12].

(4) Elastic stretch of the fiber after complete debonding is negligible, compared with slip magnitude.

Following the detailed derivation in Appendix A, we have the theoretical pullout load P versus pullout displacement δ (P-δ) relation:

$$P=\sqrt{\frac{\pi^2\tau_0 E_f d_f^3(1+\eta)}{2}\delta+\frac{\pi^2 G_d E_f d_f^3}{2}},\quad 0\le\delta\le\delta_0 \qquad (1)$$

for the debonding stage, and:

$$P=\pi d_f\tau_0\left(1+\beta(\delta-\delta_0)/d_f\right)\left(L_e-\delta+\delta_0\right),\quad \delta_0<\delta<L_e \qquad (2)$$

for the pullout stage, where L_e is the fiber embedment length and δ_0 corresponds to the displacement at which full-debonding is completed. It is given by:

$$\delta_0 = \frac{2\tau_0 L_e^2(1+\eta)}{E_f d_f} + \sqrt{\frac{8G_d L_e^2(1+\eta)}{E_f d_f}} \quad (3)$$

where $\eta = V_f E_f / V_m E_m$, V_f and V_m are the volume fractions of fiber and matrix respectively. In terms of fiber debonding length L, the debonding load P can be also expressed as:

$$P = \pi d_f \tau_0 L + \sqrt{\pi^2 G_d E_f d_f^3 / 2} \quad (4)$$

At full-debonding, $L = L_e$; hence, the maximum debonding load is given by:

$$P_a = P_b + \sqrt{\pi^2 G_d E_f d_f^3 / 2} \quad (5)$$

where $P_b = \pi d_f \tau_0 L_e$ is the initial frictional pullout load. Equation (5) can be conveniently used to calibrate the chemical bond strength G_d and frictional bond strength τ_0 from the maximum debonding load P_a and the initial frictional pullout load P_b. The slip-hardening coefficient β is obtained from (2) by best-fitting the frictional pullout portion of the P-δ curve. The dashed curve in Fig. 3 is the model result with three interfacial parameters: G_d = 6.0 J/m^2, τ_0 = 3.0 MPa and β = 0.05.

To further verify the model, the maximum debonding load P_a as a function of fiber embedment length L_e for the same PVA fiber is predicted using (5) with the same set of parameters. As can be seen from Fig. 4, good agreement between model prediction and experimental result is found.

The simple P-δ relations in equations (1) to (3) are the building blocks in constructing the composite bridging law. It is also important to study the fiber alignment effect on the pullout load and fiber in-situ strength because in an actual short fiber composite fibers are randomly oriented. The effect of fiber alignment on the pullout load, so-called "snubbing effect", was investigated in [14, 15]. An empirical relation is given by:

$$P(\phi) = P(0)e^{f\phi} \quad (6)$$

where f is the snubbing coefficient. Kanda and Li [16] investigated the effect of fiber alignment on fiber in-situ strength. Based on the experimental results for PVA fibers, a similar exponential expression was found to characterize this effect well:

$$\sigma_{fu}(\phi) = \sigma_{fu}(0)e^{-f'\phi} \quad (7)$$

where σ_{fu} is the in-situ fiber strength and f' is the fiber strength reduction coefficient. Fig. 5 shows such a fiber strength reduction effect on PVA fibers.

The parameters introduced in this section, such as the slip-hardening coefficient β, snubbing effect coefficient f, and fiber strength reduction coefficient f', are empirical, curve-fitting parameters. They are determined by single fiber pullout (straight or inclined) tests as discussed herein and in [7, 15 and 16]. The range of β for polymeric fibers such as Polypropylene, Polyethylene and PVA fibers is between 0.005 to 0.05. Snubbing coefficient f ranges from 0.5 to 0.9. The fiber strength reduction coefficient is about 0.3 for the PVA fibers, and it has not been tested for other fiber types.

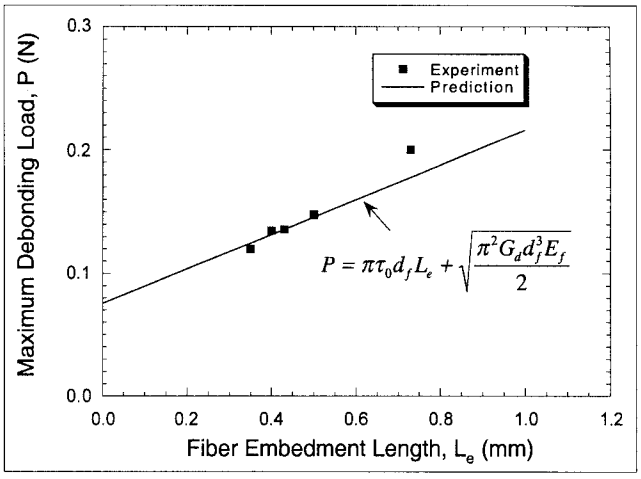

Fig. 4 – Maximum fiber debonding stress as a function of fiber embedment length for PVA (RMU) fiber: experiment vs. model prediction.

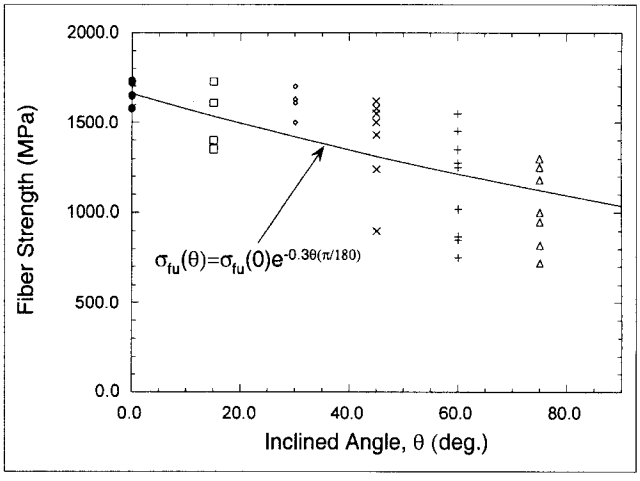

Fig. 5 – Effect of fiber inclination on in-situ fiber strength of PVA (RMU) fibers (after Kanda and Li [16]).

3. COMPOSITE BRIDGING STRESS-CRACK OPENING RELATION

Crack bridging law is a fundamental material property of fiber reinforced composites. It is cast in terms of the crack bridging stress vs. the crack opening relation (σ_B-δ relation). Based on the P-δ relation of a single fiber pullout, the composite σ_B-δ curve can be obtained by averaging over the contributions of only those individual fibers that

cross the matrix crack plane as the crack opens up [17]:

$$\sigma_B(\delta)=\frac{4V_f}{\pi d_f^2}\int_{\phi=0}^{\pi/2}\int_{z=0}^{(L_f/2)\cos\phi}P(\delta)e^{f\phi}p(\phi)p(z)dzd\phi \qquad (8)$$

where p(ϕ) and p(z) are the probability density functions of the orientation angle ϕ and the centroidal distance of a fiber from the crack plane z, respectively. The relation between decreasing fiber diameter and increasing number of fibers has been considered in the above equation. For a 3-D random distribution, $p(\phi)=\sin\phi$ and $p(z)=2/L_f$. It should be pointed out that in the crack bridging case, the crack opening δ results from two-sided fiber debonding and one-sided pullout (shorter embedment side). Therefore, P(δ) in equation (8) should be modified from the one-sided debonding result (equation (1)) as follows:

$$P=\sqrt{\pi^2E_fd_f^3\tau_0\delta(1+\eta)/4+\pi^2E_fd_f^3G_d/2} \qquad (9)$$

By changing variable, equation (8) can be re-cast into the following form[3]:

$$\sigma_B(\delta)=\frac{2V_f}{\pi d_f^2}\int_{\phi=0}^{\pi/2}\int_{\tilde{l}=0}^{1}P(\delta,\phi,\tilde{l})e^{f\phi}\sin(2\phi)d\phi d\tilde{l} \qquad (10)$$

where $\tilde{\ell}$ is normalized individual fiber embedment length (= $\ell/(L_f/2)$). In order to consider the influence of fiber rupture, when carrying out the integration (10), we need to keep discounting the contribution of broken fibers as the crack opening δ increases. To illustrate, a typical integration domain at an arbitrary crack opening δ is plotted in Fig. 6. There are several important non-dimensional variables associated with this integral domain, whose physical meanings are explained in the following:

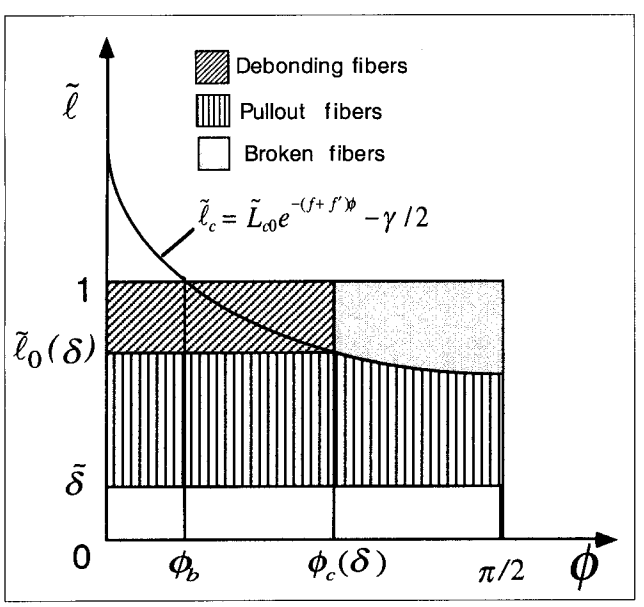

Fig. 6 – Integration domain at an arbitrary crack opening δ for normal chemical bond strength case: $\tilde{L}_c > 1$.

• Critical fiber embedment length (normalized by $L_f/2$) for individual fibers:

$$\tilde{l}_c=\tilde{L}_{c0}e^{-(f+f')\phi}-\gamma/2 \qquad (11)$$

where $\tilde{L}_{c0}=\frac{\sigma_{fu}d_f}{2\tau_0L_f}$ is the normalized critical embedment length of an aligned fiber (ϕ = 0) in absence of chemical bond [3] and $\gamma=\sqrt{8G_d/(\tau_0\delta_0^*)}$, with $\delta_0^*=\frac{\tau_0L_f^2}{E_fd_f(1+\eta)}$ is a relative measure of chemical bond strength to the frictional bond strength. Equation (11) is obtained from equations (4), (6) and (7) with P set to be the critical value $P=\pi d_f^2\sigma_{fu}(\phi)/4$. It defines the potential fiber rupture subdomain: fibers that locate above this curve will eventually rupture as a matrix crack opens up. From (11), we can define the critical fiber embedment length for aligned fiber (ϕ = 0) with both chemical bond and frictional bond:

$$\tilde{L}_c=\tilde{L}_{c0}-\gamma/2 \qquad (12)$$

Fibers at all orientation angles have the potential to rupture if its half-length $L_f/2 > L_c$ (i.e. $\tilde{L}_c < 1$). Clearly, chemical bond tends to promote fiber rupture. Also, by setting ϕ = π/2 in (11), another limiting fiber length can be defined:

$$\tilde{L}_r=2\tilde{L}_{c0}e^{-(f+f')\pi/2}-\gamma \qquad (13)$$

If $L_r > L_f$ (*i.e.* $\tilde{L}_r > 2$), no fiber rupture will occur regardless of orientation angle. Also in Fig. 6, the variable $\tilde{\ell}_0(\delta) = \tilde{\ell}_c(\phi = \phi_c)$ defines the critical embedment length at which debonding of the fiber has completed at crack opening δ and just survived rupture.

• For fiber length between L_r and $2L_c$, some fibers will rupture, depending on their orientation angles. The limiting fiber rupture angle ϕ_b:

$$\phi_b=-\frac{1}{f+f'}\ln\left(\frac{1}{\tilde{L}_{c0}}+\frac{\gamma}{2\tilde{L}_{c0}}\right),\quad 0\le\phi_b\le\pi/2 \qquad (14)$$

defines the potential fiber rupture space in terms of orientation angle: only those fibers orient at an angle higher than ϕ_b will eventually rupture.

• Current fiber rupture angle $\phi_c(\delta)$:

$$\phi_c(\delta)=-\frac{1}{2(f+f')}\ln\left(\frac{\delta}{\tilde{L}_{c0}^2\delta_0^*}+\frac{\gamma^2}{4\tilde{L}_{c0}^2}\right) \qquad (15)$$

It defines the fiber orientation angle above which fibers must have ruptured at a given crack opening (the driving force for fiber rupture). This quantity is bounded between ϕ_b and π/2. As crack opening δ increases, ϕ_c starts from π/2 and approaches ϕ_b. Note that within the potential fiber rupture space, whether a specific fiber will rupture or not still depends on its embeddment length.

Equation (15) is generally not applicable to ductile metal fibers due to the elasticity assumption in its derivation. For ductile fibers, if not too far beyond yielding is expected, (15) could be a good estimation.

Based on Fig. 6, it is not difficult to evaluate the left-hand side of (10) analytically by taking only the shaded domains marked as debonding and pullout fibers in the figure. Fibers that have broken or have been pulled-out (embedment length less that crack opening) are eliminated. Closed-form expressions for the crack bridging are included in Appendix B, which form the theoretical basis for discussions in the following sections. For more detailed derivation, one may refer to the previous works [3] and [16].

It is worth considering a special case of extremely strong chemical bonding ($\gamma >> 1$). In this case, part or all of fibers will rupture either during the debonding process or even before debonding (recall that there is a threshold for initiation of debonding governed by chemical bond strength (ref. equation (1)). Fig. 7 shows such a case. Fibers belonging to $\phi_r < \phi < \pi/2$ and $0 < \ell < 1$ will rupture during the debonding initiation process, where ϕ_r is given by:

$$\phi_r = -\frac{1}{f+f'} \ln\left(\frac{\gamma}{2\tilde{L}_{c0}}\right) \tag{16}$$

The maximum bridging stress is attained at the initial stage ($\delta = 0$), and it can be estimated by summing the contributions from debonding and non-debonding (rupture before debonding) fibers:

$$\sigma_B = \frac{V_f}{2}\int_0^{\phi_r}\int_0^1 \sigma_{d0} e^{f\phi} \sin 2\phi d\tilde{l} d\phi + \frac{V_f}{2}\int_{\phi_r}^{\pi/2}\int_0^1 \sigma_{fu} e^{-f'\phi} \sin 2\phi d\tilde{l} d\phi \tag{17}$$

where $\sigma_{d0} = \dfrac{2\sigma_0\gamma}{V_f}$ and $\sigma_0 = 1/2 V_f \tau_0 \left(L_f/d_f\right)$. It results in:

$$\sigma_B = \frac{V_f\sigma_{fu}}{2}\left[\frac{2e^{-2f'\pi/2} + e^{-f'\phi_r}\left(f'\sin 2\phi_r + 2\cos 2\phi_r\right)}{4+f'^2}\right] + \sigma_0\gamma\left[\frac{2+e^{f\phi_r}\left(f\sin 2\phi_r - 2\cos 2\phi_r\right)}{4+f^2}\right] \tag{18}$$

Figs. 8 to 12 show graphically the non-dimensional crack bridging stress - crack opening curves derived analytically. Figs. 8 and 9 are the pre-fully-debonding curves for fiber/matrix systems with low tendency of fiber rupture ($\tilde{L}_{c0} = 2.0$) and high tendency of fiber rupture ($\tilde{L}_{c0} = 0.5$). In both Figs. 8 and 9, the parameter $\gamma / \tilde{L}_{c0}$ (from 0.0 to 0.9) indicates the relative chemical bond strength,

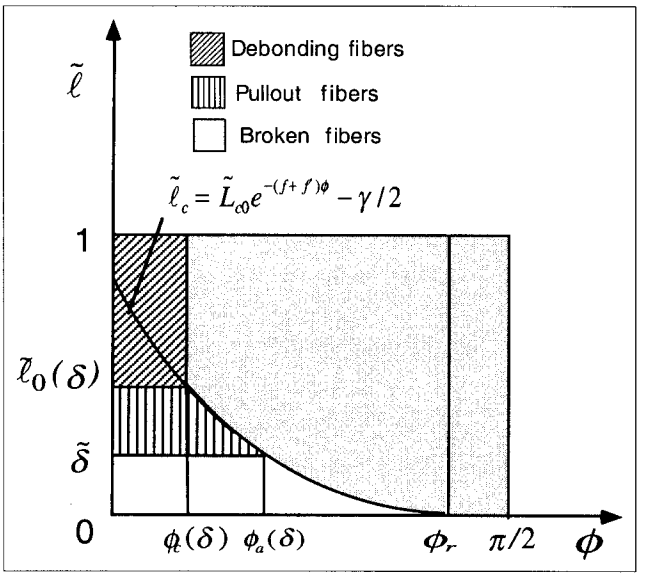

Fig. 7 – Integration domain at an arbitrary crack opening δ for extreme chemical bond strength case: $\tilde{L}_c < 1$, $\tilde{L}_r < 0$.

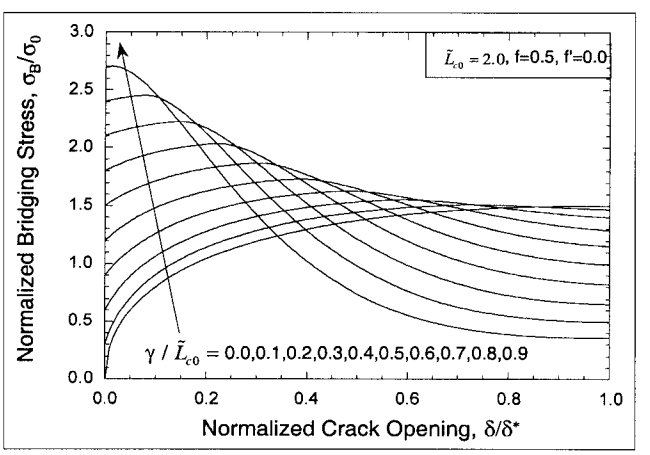

Fig. 8 – Pre-fully-debonding bridging stress - crack opening curves for a system with low tendency of fiber rupture.

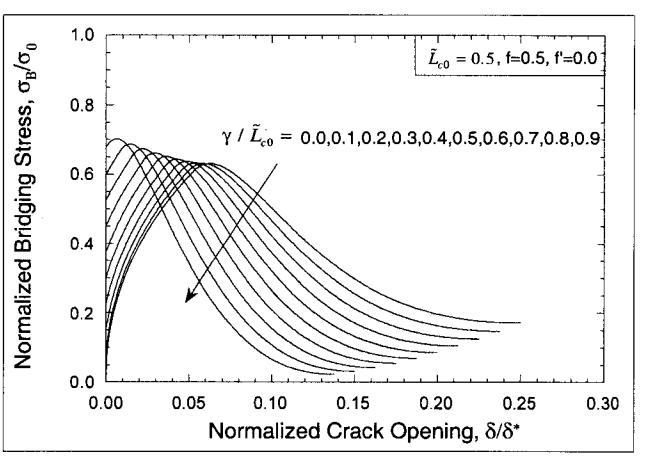

Fig. 9 – Pre-fully-debonding bridging stress - crack opening curves for a system with high tendency of fiber rupture.

given other fiber and interface characteristics such as fiber length, diameter, strength and frictional bond strength. It can be seen from these two figures, chemical

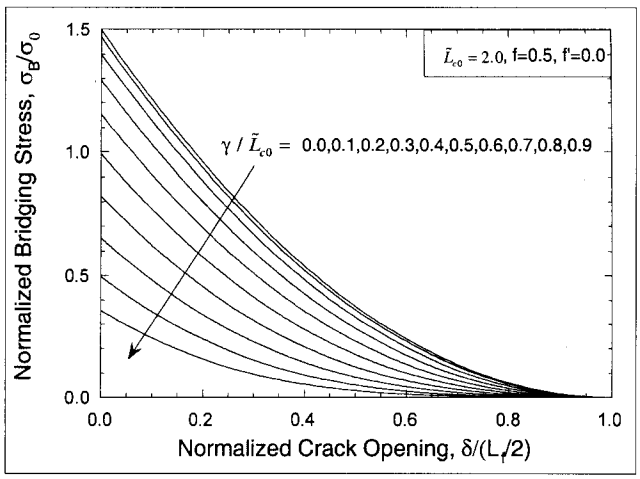

Fig. 10 – Post-fully-debonding bridging stress - crack opening curves for a system with low tendency of fiber rupture (continuation of the curves in Fig. 8).

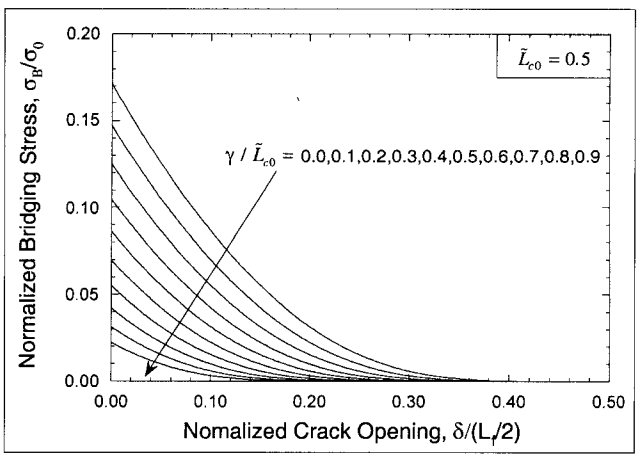

Fig. 11 – Post-fully-debonding bridging stress - crack opening curves for a system with high tendency of fiber rupture (continuation of the curves in Fig. 9).

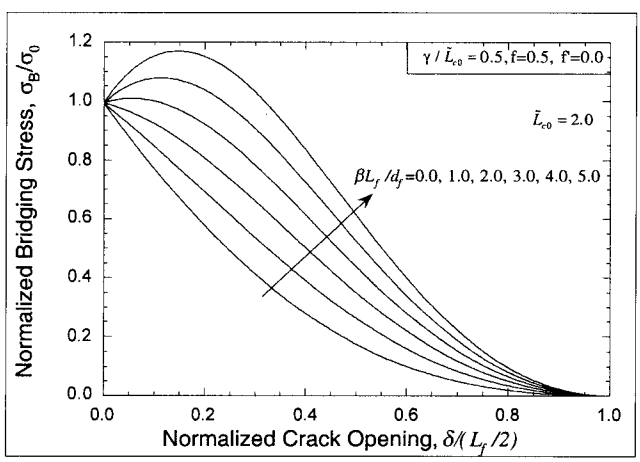

Fig. 12 – Effect of slip-hardening interface on the post-fully-debonding σ_B-δ relation.

bond tends to increase initial bridging stress and reduce the complementary area to the left of the σ_B-δ curve up to the maximum bridging stress point (this area is referred as the complementary energy [4]). When fiber rupture tendency is low, chemical bond increases the maximum bridging stress much more dramatically than the case with high fiber rupture tendency ($\tilde{L}_{c0}$ = 0.5). Also, at the end of debonding stage, because of less severe fiber rupture, the bridging stress remains higher at a larger corresponding crack opening in $\tilde{L}_{c0}$ = 2.0 case. This also contributes to larger post-debonding fracture energy - area under the descending part of the σ_B-δ curve (see Figs. 10 and 11). In the case of slip-hardening (Fig. 12), both bridging stress and fracture energy can be further increased, depending on the slip-hardening coefficient.

4. MODEL IMPLICATIONS ON MATERIALS DESIGN FOR DESIRED PROPERTIES

With the analytical tools developed, it is convenient to predict the composite overall properties from its constituents - fiber, matrix and interface. In this section, some direct implications from the current micromechanics model are presented, including tensile strength, fracture energy and complementary energy (a measure of material ductility).

Tensile Strength, Fracture Energy, Ductility

The tensile strength predicted by the model is essentially the maximum bridging stress for a fiber/cement composite which shows multiple cracking (ref. [18]). Fig. 13 shows the dependency of tensile strength on fiber length in a non-dimensional form. Given fiber volume fraction V_f, diameter d_f, fiber strength σ_{fu} and frictional bond strength τ_0, the composite tensile strength σ_{cu} monotonically increases with fiber length in zero chemical bonding case (the lowest curve in Fig. 13). This is consistent with the result derived by

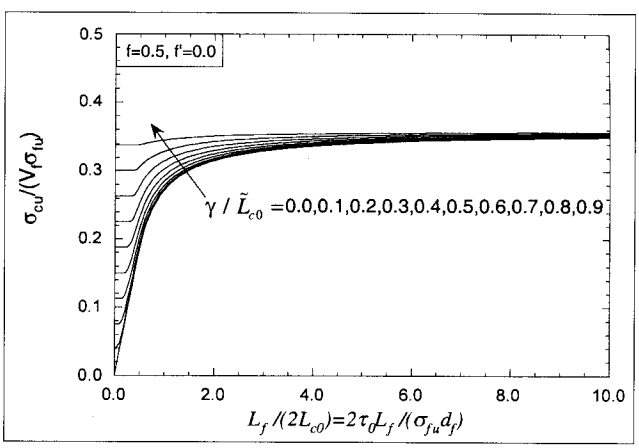

Fig. 13 – Normalized composite tensile strength as a function of normalized fiber length and relative chemical bond strength.

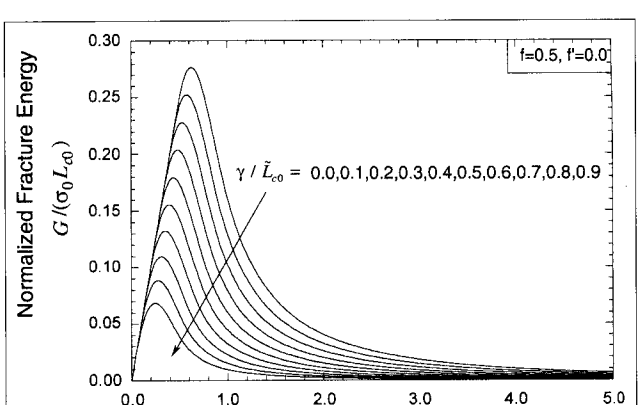

Fig. 14 – Normalized composite fracture energy as a function of normalized fiber length and relative chemical bond strength.

Maalej *et al.* [3]. As chemical bond increases, tensile strength for short fiber length can be dramatically increased. The plateaus at small fiber lengths indicate that composite tensile strength is controlled by the initial debonding stress which is in turn governed by chemical bond. As fiber becomes longer, subsequent debonding after initial debonding results in higher bridging stress and composite tensile strength. From this figure, it is clear that when fiber is too long or chemical bond is too strong, composite tensile strength becomes almost independent of fiber length. Physically, those two limiting cases lead to severe fiber rupture and composite tensile strength should be mainly controlled by fiber volume fraction and fiber strength.

Shown in Fig. 14 is composite fracture energy as a function of fiber length and the relative chemical bond strength. This fracture energy is the energy absorbed by bridging fibers in the crack plane and it is evaluated by integrating the area under the post-fully-debonding portion of a bridging stress - crack opening curve (Figs. 10-11). The peak shown in each curve in Fig. 14 indicates that there exists an optimal fiber length to maximize the fracture energy of a fiber composite. It is also clear that chemical bond tends to reduce fracture energy because it promotes more fiber rupture.

The concept of multiple cracking in fiber reinforced brittle matrix composites has been extensively studied. Marshall and Cox [18] proposed a simple means of determining the condition for steady state cracking, required for multiple cracking. Based on a J-integral analysis, the condition can be written in terms of the complementary energy G_c and the crack tip toughness J_0:

$$G_c \geq J_0 \tag{19}$$

where G_c is defined in terms of fiber bridging property via the σ_B-δ curve:

$$G_c = \sigma_{cu}\delta_{cu} - \int_0^{\delta_{cu}} \sigma_B(\delta)d\delta \tag{20}$$

and σ_{cu} and δ_{cu} are the maximum bridging stress and the corresponding crack opening. Graphically, G_c is simply the complementary area to the left of the σ_B-δ curve up to peak stress.

The above discussion suggests that high ductility of a short fiber composite requires large complementary energy. Equation (19) becomes a very important design criterion for ductile fiber composites. Using the generic micromechanics model developed in this research, one can easily compute this quantity with different combinations of fiber, matrix and interface properties and choose the one that satisfies condition (19) to guarantee the ductility of such engineered fiber composites. Shown in Fig. 15 are the normalized complementary energy as a function of fiber length and relative chemical bond strength.

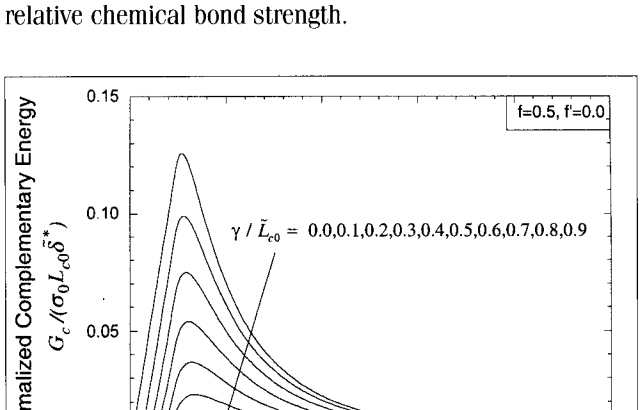

Fig. 15 – Normalized composite complementary energy as a function of normalized fiber length and relative chemical bond strength.

An Example - PVA fiber/cement composites

Recently, Polyvinyl Alcohol (PVA) fiber has been recognized for its high potential as reinforcement in high performance cementitious composites due to its high strength. This type of fiber can also form strong chemical bond to the cement matrix. In order to maximize the potential of PVA fibers as viable reinforcement for cement based composites which have both high strength and high ductility, analytical material design tools are certainly needed. To demonstrate the usefulness of the present micromechanics model, two types of cement composites made from two types of PVA fibers (RMU and RK with 14 and 40 μm diameter respectively) are investigated.

Table 1 lists the fiber and interface parameters for both PVA fibers. The interfacial properties were derived from the simple fiber pullout tests discussed previously. PVA-RMU composite contains 1.5% volume fraction of RMU fibers while PVA-RK composite has 2% RK fibers.

Table 1 – Fiber and interfacial parameters for PVA-RMU and RK fibers

Fiber Type	E_f (GPa)	L_f (mm)	d_f (μm)	τ_0 (MPa)	G_d (Nm)	σ_{fu} (MPa)	f, f'
RMU	60	6	14	3.0	6.0	1660	0.5, 0.3
RK	22	12	40	2.0	6.0	860	0.5, 0.3

Table 2 – Matrix mix proportion

Cement	Sand	Water	Super Plasticizer	Viscous Agent
1.0	0.4	0.45	0.02	0.002

The matrix mix proportion for the two composites are listed in Table 2. They were tested after seven days water curing and one day air drying. Standard dog-bone shaped specimens were used.

Fig. 16 shows the uniaxial tension test results for both composites. As can be seen from this figure, PVA-RMU has higher tensile strength but much lower ductility than the PVA-RK composite. This is because RMU fiber is much thinner in diameter. Although it is a higher fiber strength than the RK fiber, under similar interfacial conditions, RMU fibers suffered more severe fiber rupture, which leads to lower ductility. The contrast in ductility between these two composites can be explained more clearly using the complementary concept later on.

Fig. 17 shows the comparison between model predictions and tensile test results in terms of tensile strength. The model predicts higher tensile strength for PVA-RMU than for PVA-RK, consistent with experimental observations. Note however, that the PVA-RMU does not satisfy the multiple cracking condition (equation (19)) (see discussion to follow) and the measured tensile strength cannot be expected to be the same as the calculated maximum bridging stress. Also, the current tensile strengths for both composites are very close to their limit values and reduction in fiber length will not cause much loss in tensile strength. From the fracture energy predictions (Fig. 18), the current fiber lengths (12 mm for RK, 6 mm for RMU) are well over the optimal values for maximum fracture energy. The difference in tensile strength as L_f approaches zero is due to the fiber strength difference.

Fig. 19 illustrates the complementary energy as a function of fiber length for both composites. Under current composite design, PVA-RK has a G_c value of 3.4 J/m^2 while PVA-RMU has only 0.8 J/m^2. Compared to the fracture toughness of cement paste, which is about 2 J/m^2, the PVA-RK composite satisfies the multiple cracking condition (19) and this is the reason behind the contrast in tensile ductility of the two composites.

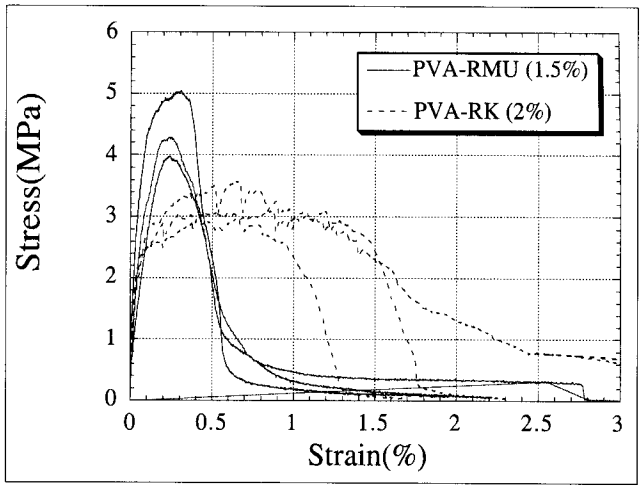

Fig. 16 – Uniaxial tensile test results for PVA-RMU and PVA-RK composites.

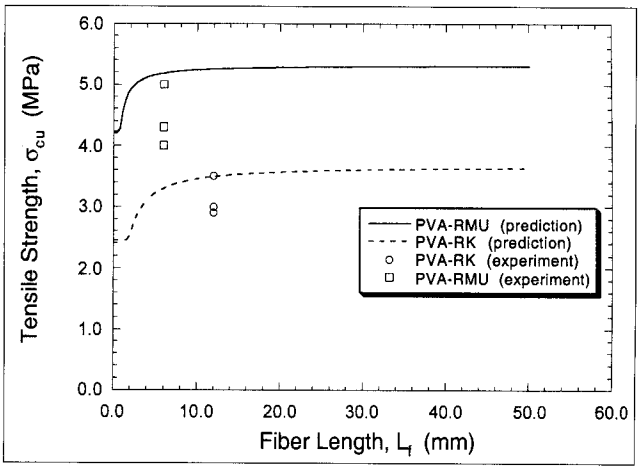

Fig. 17 – Composite tensile strength as a function of fiber length for both PVA-RMU and RK composites: experiments vs model predictions.

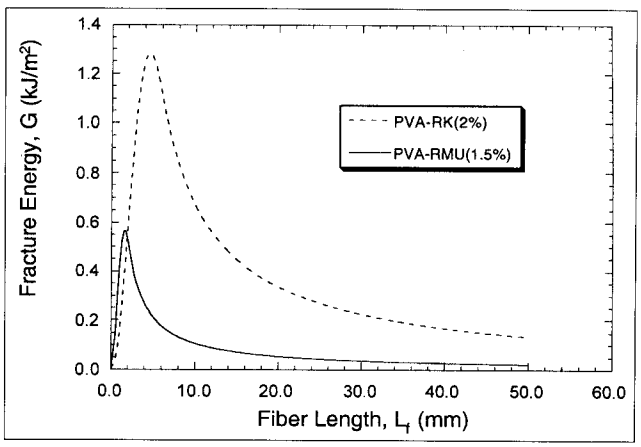

Fig. 18 – Predicted composite fracture energy as a function of fiber length for both PVA-RMU and RK composites.

Fig. 20 shows the effect of chemical bond strength G_d on both fracture energy and tensile strength of the PVA-RMU composite. Clearly, chemical bond decreases the fracture energy dramatically while increases the tensile

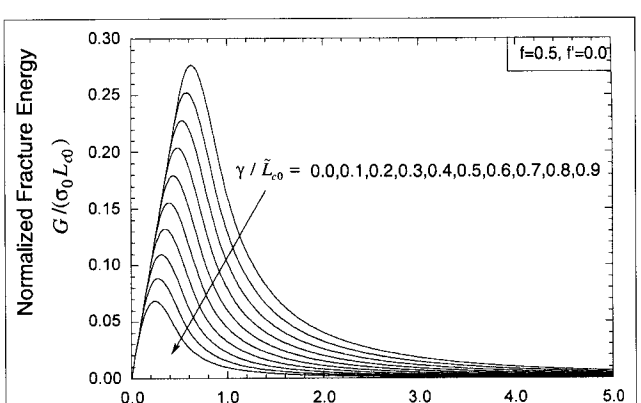

Fig. 14 – Normalized composite fracture energy as a function of normalized fiber length and relative chemical bond strength.

Maalej *et al.* [3]. As chemical bond increases, tensile strength for short fiber length can be dramatically increased. The plateaus at small fiber lengths indicate that composite tensile strength is controlled by the initial debonding stress which is in turn governed by chemical bond. As fiber becomes longer, subsequent debonding after initial debonding results in higher bridging stress and composite tensile strength. From this figure, it is clear that when fiber is too long or chemical bond is too strong, composite tensile strength becomes almost independent of fiber length. Physically, those two limiting cases lead to severe fiber rupture and composite tensile strength should be mainly controlled by fiber volume fraction and fiber strength.

Shown in Fig. 14 is composite fracture energy as a function of fiber length and the relative chemical bond strength. This fracture energy is the energy absorbed by bridging fibers in the crack plane and it is evaluated by integrating the area under the post-fully-debonding portion of a bridging stress - crack opening curve (Figs. 10-11). The peak shown in each curve in Fig. 14 indicates that there exists an optimal fiber length to maximize the fracture energy of a fiber composite. It is also clear that chemical bond tends to reduce fracture energy because it promotes more fiber rupture.

The concept of multiple cracking in fiber reinforced brittle matrix composites has been extensively studied. Marshall and Cox [18] proposed a simple means of determining the condition for steady state cracking, required for multiple cracking. Based on a J-integral analysis, the condition can be written in terms of the complementary energy G_c and the crack tip toughness J_0:

$$G_c \geq J_0 \tag{19}$$

where G_c is defined in terms of fiber bridging property via the σ_B-δ curve:

$$G_c = \sigma_{cu}\delta_{cu} - \int_0^{\delta_{cu}} \sigma_B(\delta)d\delta \tag{20}$$

and σ_{cu} and δ_{cu} are the maximum bridging stress and the corresponding crack opening. Graphically, G_c is simply the complementary area to the left of the σ_B-δ curve up to peak stress.

The above discussion suggests that high ductility of a short fiber composite requires large complementary energy. Equation (19) becomes a very important design criterion for ductile fiber composites. Using the generic micromechanics model developed in this research, one can easily compute this quantity with different combinations of fiber, matrix and interface properties and choose the one that satisfies condition (19) to guarantee the ductility of such engineered fiber composites. Shown in Fig. 15 are the normalized complementary energy as a function of fiber length and relative chemical bond strength.

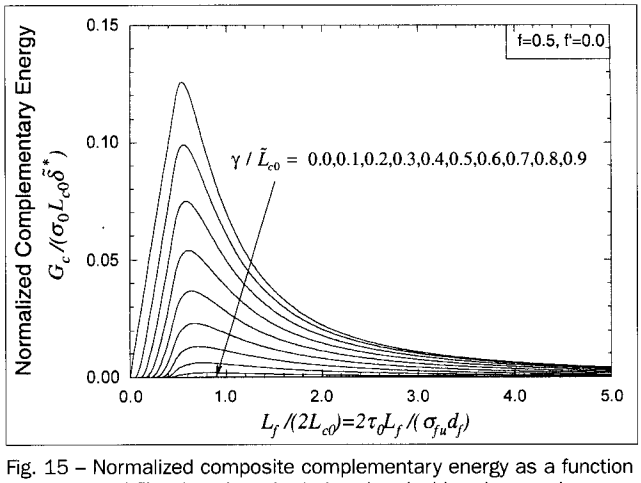

Fig. 15 – Normalized composite complementary energy as a function of normalized fiber length and relative chemical bond strength.

An Example - PVA fiber/cement composites

Recently, Polyvinyl Alcohol (PVA) fiber has been recognized for its high potential as reinforcement in high performance cementitious composites due to its high strength. This type of fiber can also form strong chemical bond to the cement matrix. In order to maximize the potential of PVA fibers as viable reinforcement for cement based composites which have both high strength and high ductility, analytical material design tools are certainly needed. To demonstrate the usefulness of the present micromechanics model, two types of cement composites made from two types of PVA fibers (RMU and RK with 14 and 40 μm diameter respectively) are investigated.

Table 1 lists the fiber and interface parameters for both PVA fibers. The interfacial properties were derived from the simple fiber pullout tests discussed previously. PVA-RMU composite contains 1.5% volume fraction of RMU fibers while PVA-RK composite has 2% RK fibers.

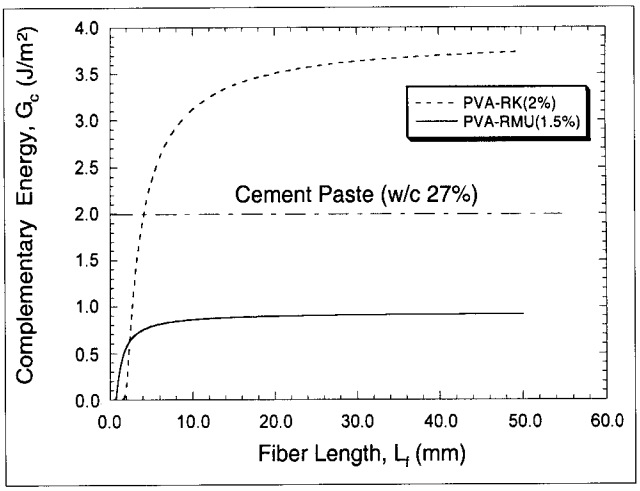

Fig. 19 – Predicted composite complementary energy as a function of fiber length for both PVA-RMU and RK composites.

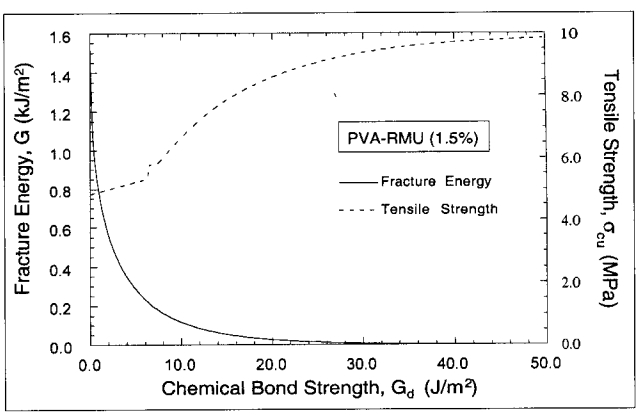

Fig. 20 – Predicted composite fracture energy and tensile strength as a function of chemical bond strength for the PVA-RMU composite.

strength to the limit set by fiber strength and volume fraction. The kink in the tensile strength curve is due to the transition from normal chemical bonding to extreme chemical bonding case as discussed previously (Ref. equation (18)). It is important to tailor the interfacial properties including chemical bond to achieve both high strength and high ductility.

4. CONCLUSIONS AND DISCUSSIONS

(1) Several important interfacial behaviors characterized: chemical bond, frictional bond, and slip-hardening. These interfacial parameters can be determined from a single fiber pullout test.

(2) An analytical bridging stress-crack opening relation is derived, which can be used as a materials design tool for desired properties and cost-effectiveness *via* intelligent fiber selection (type, strength, length, content,...), matrix modification and fiber/matrix interface tailoring.

(3) *Via* parametric study presented in this paper, it is found that in fiber rupture cases, interfacial fracture toughness (chemical bond) tend to increase composite tensile strength but decreases composite fracture energy and complementary energy as well as ductility.

Single fiber pullout problem is a complicated solid mechanics problem. The derivation included in the present study is only an approximate solution to this complicated problem, based on simplified force and energy balance. The attempt has been made to capture the physical essence of the interfacial parameters in a simple, easy-to-use formulation without getting into complex mathematics. In the current micromechanics model, the fiber dispersion effect and the statistical distribution of fiber strength are not included. The comparison between the two fiber/cement composites PVA-RMU and PVA-RK is meant to demonstrate the usefulness of the model in fiber section for desired properties (say, ductility) rather than just a comparision, which has been the central theme of this work.

ACKNOWLEDGMENTS

Support of this work has been provided by the National Science Foundation (CMS-9601262) to the University of Michigan.

REFERENCES

[1]Krenchel, H. and Hansen, S., 'New recipes and new production techniques for high performance FRC-materials', in 'High Performance Fiber Reinforced Cement Composites', Reinhardt H. W., Naaman, A. E., Eds., E& FN Spon, London, 1992, pp 65-83.

[2] Naaman, A. E., 'SIFCON: Tailored properties for structural performance', in 'High Performance Fiber Reinforced Cement Composites', Reinhardt H. W, Naaman, A. E., Eds., E& FN Spon, London, 1992; pp 18-38.

[3] Maalej M., Li, V. C. and Hashida, T., 'Design and Structural Applications of Stress-Crack Width Relations' in 'Fiber Reinforced Concrete', *J. of Engineering Mechanics* **8** (1995) 903-913.

[4] Li, V. C., Kanda, T. and Lin, Z., 'The Influence of Fiber/Matrix Interface Properties on Complementary Energy and Composite Damage Tolerance', in Key Engineering Materials: Proc. 3rd Conf. on Frac. & Strength of Solids, Hong Kong, 1997, pp 465-472.

[5] Li, V. C. and Leung, C. K. Y., 'Steady state and multiple cracking of short random fiber composites', *ASCE J. Engng Mech.* **118** (1992) 2246-2264.

[6] Li, V. C. and Wu, H. C., 'Conditions for pseudo strain-hardening' in 'Fiber Reinforced Brittle Matrix Composites', *J. Appl. Mech. Rev.* **45** (8) (1992) 390-398.

[7] Lin, Z. and Li, V. C., 'Crack bridging in fiber reinforced cementitious composites with slip-hardening interfaces', *J.*

Mech. Phys. Solids **45** (5) (1997) 763-787.

[8] Li, V. C. and Kanda, T., 'Engineered cementitious composites for structural applications', *ASCE J. Mater. Civil Eng.* **10** (2) (1998) 66-69.

[10] Kabele, P., Li, V. C., Horii, H., Kanda, T. and Takeuchi, S., 'Use of BMC for Ductile Structural Members', in Proc. of 5th Int. Sym. on Brittle Matrix Composites, Warsaw, Poland, 1997; pp. 579-588.

[10] Kanda, T., Watanabe, S. and Li, V. C., 'Application of Pseudo Strain Hardening Cementitious Composites to Shear Resistant Structural Elements', in Proc. Fracture Mechanics of Concrete Structures-3, AEDIFICATIO Publishers, Freiburg, Germany, Oct., 1998, pp. 1477-1490.

[11] Li, V. C., 'From micromechanics to structural engineering - the design of cementitious composites for civil engineering applications', *JSCE J. Struct. Mech. Earthquake Eng.* **10** (2) (1993) 37-48.

[12] Wang, Y., Li, V. C. and Backer, S., 'Modeling of fiber pull-out from a cement matrix', *Int'l. J. Cement Comp. Lightweight Concrete* **10** (3) (1988) 143-149.

[13] Katz, A., Li, V. C., 'A Special technique for determining the bond strength of carbon fibers in cement matrix by pullout test', *J. Materials Science Letters* **15** (1996) 1821-1823.

[14] Morton, J. and Groves, G. W., 'The effect of metal wires on the fracture of a brittle matrix composite', *J. Mater. Sci.* **11** (1976) 617-622.

[15] Li, V. C., 'Post-crack scaling relations for fiber reinforced cementitious composites', *ASCE J. Mater. Civil Engng.* **4** (1) (1992) 41-57.

[16] Kanda, T. and Li, V. C., 'Interface property and apparent strength of a high strength hydrophilic fiber in cement matrix', *ASCE J. Mater. Civil Engng.* **10** (1) (1998) 5-13.

[17] Li, V. C., Wang, Y. and Backer, S., 'A micromechanical model of tension-softening and bridging toughening of short random fiber reinforced brittle matrix composites', *J. Mech. Phys. Solids* **39** (5) (1991) 607-625.

[18] Marshall, D. B. and Cox, B. N., 'A J-integral method for calculating steady-state matrix cracking stress in composites', *Mech. Mater.* 7 (1988) 127-133.

[19] Gao, Y. C., Mai, Y.-W. and Cotterell, B., 'Fracture of fiber-reinforced materials', *J. Appl. Math. Phys.* **39** (1988) 550-558.

APPENDIX

Appendix A

Derivation of P-δ relation with combined chemical bond and frictional bond

Consider a fiber with length L_e embedded in a matrix (Fig. A1). A portion of the fiber/matrix interface is debonded. The debonded zone length is L, within which a constant frictional stress τ_0 is assumed to exist. Chemical bond strength for the bonded region is G_d. The task here is to derive the relation between fiber pullout load P or stress σ and fiber pullout displacement δ.

From equilibrium requirements, the one-dimensional

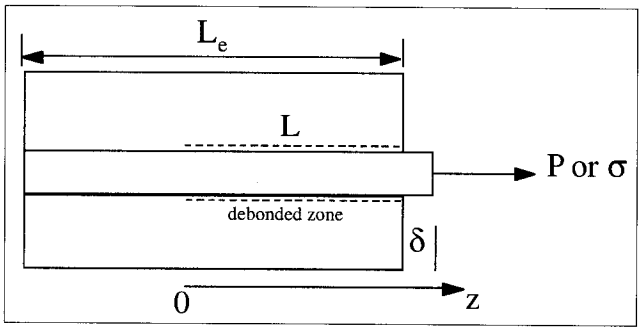

Fig. A1.

stress distribution in the debonded region is given by:

$$\sigma_f(z) = \sigma_{f0} + \frac{z(\sigma - \sigma_{f0})}{L} \tag{A-1}$$

$$\sigma_m(z) = (1 - z/L)\sigma_{m0} \tag{A-2}$$

where σ_{f0} and σ_{m0} are the normel stresses in the fiber and the matrix respectively at z = 0, and they are given by:

$$\sigma_{f0} = \sigma - \frac{4\tau_0 L}{d_f} \tag{A-3}$$

$$\sigma_{m0} = \frac{4\tau_0 L V_f}{d_f V_m} \tag{A-4}$$

where V_f and V_m are the volume fractions of fiber and matrix respectively.

Define the relative displacement between fiber and matrix in the debonded region as:

$$\Delta(z) = u_f(z) - u_m(z) \tag{A-5}$$

Then,

$$\frac{d\Delta(z)}{dz} = \frac{du_f(z)}{dz} - \frac{du_m(z)}{dz} = \frac{\sigma_f(z)}{E_f} - \frac{\sigma_m(z)}{E_m} \tag{A-6}$$

Substituting (A-1) through (A-4) and applying the boundary condition Δ(z = 0) = 0, we have:

$$\Delta z = \frac{\sigma z}{E_f} - \frac{4\tau_0 L z}{E_f d_f}(1+\eta) + \frac{2\tau_0 z^2}{E_f d_f}(1+\eta) \tag{A-7}$$

where $\eta = \frac{V_f E_f}{V_m E_m}$. The fiber pullout distance is then given by

$$\delta = \Delta(L) = \frac{\sigma L}{E_f} - \frac{2\tau_0 L^2 (1+\eta)}{E_f d_f} \tag{A-8}$$

Now, we need to find $\sigma = \sigma(L, G_d, \tau_0, \ldots)$. An energy based debonding criterion is employed in establishing such a relation [19].

For any infinitesimal advance of the debonded zone, dA, the energy conservation requires

$$Pdu_f = dU + dW_f + G_d dA \tag{A-9}$$

where u_f is the axial displacement at the pulled fiber end (work conjugate of applied load $P = \pi d_f^2 \sigma / 4$), dU is the change in strain energy in the system, dW_f is the change in energy dissipated by friction at the interface, and $G_d dA$ is the energy consumed in the advance of debonded zone. On the other hand, if the debonded zone is considered as a stress boundary of the system, it can be shown that [19]:

$$dU = \frac{1}{2}\left(Pdu_f - dW_f\right) \tag{A-10}$$

From (A-9) and (A-10), we have:

$$G_d dA = \frac{1}{2}\left(Pdu_f - dW_f\right) \tag{A-11}$$

where u_f and W_f can be obtained from:

$$u_f = \int_0^L \frac{\sigma_f(z)}{E_f} dz + \frac{V_f \sigma}{E_c}\left(L_e - L\right) \tag{A-12}$$

and

$$W_f = \int_0^L \pi d_f \tau_0 \Delta(z) dz \tag{A-13}$$

In equation (A-12),

$$E_c = V_f E_f + V_m E_m \tag{A-14}$$

By using relevant equations already derived, (A-11) becomes:

$$\sigma^2 - \frac{8\tau_0 L(1+\eta)}{d_f}\sigma + \frac{16\tau_0^2 L^2 (1+\eta)^2}{d_f^2} - \frac{8G_d E_f (1+\eta)}{d_f} = 0 \tag{A-15}$$

It follows that

$$\sigma = \frac{4\tau_0 L(1+\eta)}{d_f} + \sqrt{\frac{8G_d E_f (1+\eta)}{d_f}} \tag{A-16}$$

or:

$$P = \pi d_f^2 \sigma / 4 = \pi d_f \tau_0 L(1+\eta) + \sqrt{\frac{\pi^2 G_d d_f^3 E_f (1+\eta)}{2}} \tag{A-17}$$

In a single fiber pullout specimen, η can be neglected without losing accuracy. Therefore, equation (5) in the main text results from (A-17). Also, when $L = L_e$, maximum debonding load is reached. The corresponding displacement is given by (A-16) and (A-8):

$$\delta_0 = \frac{2\tau_0 L_e^2 (1+\eta)}{E_f d_f} + \sqrt{\frac{8G_d L_e^2 (1+\eta)}{E_f d_f}} \tag{A-18}$$

Combining (A-17) and (A-8), we have:

$$P = \sqrt{\frac{\pi^2 \tau_0 E_f d_f^3 (1+\eta)}{2}}\delta + \frac{\pi^2 G_d E_f d_f^3}{2} \tag{A-19}$$

If $\eta = 0$, (A-19) reduces to equation (2) in the main text.

After debonding, the interface is controlled by frictional bond only. By taking $S = \delta - \delta_0$ in equation (1) in the main text and from force balance, it is readily shown that for fiber pullout stage,

$$P = \pi d_f \tau_0 \left(1 + \beta(\delta - \delta_0)/d_f\right)\left(L_e - \delta + \delta_0\right) \tag{A-20}$$

Appendix B Analytical crack bridging relation

For $L_r < L_f < 2L_c$

$$\frac{\sigma_B}{\sigma_0} \begin{cases} g\left[\sqrt{4(1+\gamma)\frac{\tilde{\delta}}{\tilde{\delta}^*} + \gamma^2} - (1+\gamma)\frac{\tilde{\delta}}{\tilde{\delta}^*}\right] & 0 \le \tilde{\delta} \le \tilde{\delta}_u\left(\phi = \frac{\pi}{2}\right) \\ G(\phi_c, f)\left[\sqrt{4(1+\gamma)\frac{\tilde{\delta}}{\tilde{\delta}^*} + \gamma^2} - (1+\gamma)\frac{\tilde{\delta}}{\tilde{\delta}^*}\right] + \tilde{L}_{c0}^2 A(\phi_c, -f-2f') & \\ -\tilde{L}_{c0}\gamma A(\phi_c, -f') + \frac{1}{4}\gamma^2 A(\phi_c, f) & \tilde{\delta}_u\left(\phi = \frac{\pi}{2}\right) \le \tilde{\delta} \le \tilde{\delta}^* \\ \left\{G(\phi_b, f)(1-\tilde{\delta})^2 + \tilde{L}_{c0}^2 A(\phi_b, -f-2f') - 2\tilde{L}_{c0}\left(\tilde{\delta} + \frac{\gamma}{2}\right)A(\phi_b, -f')\right. & \\ \left. + \left(\tilde{\delta} + \frac{\gamma}{2}\right)^2 A(\phi_b, f)\right\}(1 + c\tilde{\delta}) & \tilde{\delta}^* \le \tilde{\delta} \le \frac{\tilde{L}_r}{2} \\ \left\{G(\phi_b, f)(1-\tilde{\delta})^2 + \tilde{L}_{c0}^2 B(\phi_b, \phi_a, -f-2f') - 2\tilde{L}_{c0}\left(\tilde{\delta} + \frac{\gamma}{2}\right)B(\phi_b, \phi_a, -f')\right. & \\ \left. + \left(\tilde{\delta} + \frac{\gamma}{2}\right)^2 B(\phi_b, \phi_a, f)\right\}(1 + c\tilde{\delta}) & \frac{\tilde{L}_r}{2} \le \tilde{\delta} \le 1 \end{cases}$$

For $L_f > 2L_c$

$$\frac{\sigma_B}{\sigma_0}\begin{cases} g\left[\sqrt{4(1+\gamma)\frac{\tilde{\delta}}{\tilde{\delta}^*}+\gamma^2}-(1+\gamma)\frac{\tilde{\delta}}{\tilde{\delta}^*}\right] & 0\le\tilde{\delta}\le\tilde{\delta}_u\left(\phi=\frac{\pi}{2}\right) \\ G(\phi_c,f)\left[\sqrt{4(1+\gamma)\frac{\tilde{\delta}}{\tilde{\delta}^*}+\gamma^2}-(1+\gamma)\frac{\tilde{\delta}}{\tilde{\delta}^*}\right]+\tilde{L}_{c0}^2A(\phi_c,-f-2f') & \\ -\tilde{L}_{c0}\gamma A(\phi_c,-f')+\frac{1}{4}\gamma^2A(\phi_c,f) & \tilde{\delta}_u\left(\phi=\frac{\pi}{2}\right)\le\tilde{\delta}\le\tilde{\delta}_u(\phi=0) \\ \left\{\tilde{L}_{c0}^2G\left(\frac{\pi}{2},-f-2f'\right)-2\tilde{L}_{c0}\left(\tilde{\delta}+\frac{\gamma}{2}\right)G\left(\frac{\pi}{2},-f'\right)\right. & \\ \left.+\left(\tilde{\delta}+\frac{\gamma}{2}\right)^2G\left(\frac{\pi}{2},f\right)\right\}(1+c\tilde{\delta}) & \tilde{\delta}_u(\phi=0)\le\tilde{\delta}\le\frac{\tilde{L}_r}{2} \\ \left\{\tilde{L}_{c0}^2G(\phi_a,-f-2f')-2\tilde{L}_{c0}\left(\tilde{\delta}+\frac{\gamma}{2}\right)G(\phi_a,-f')\right. & \\ \left.+\left(\tilde{\delta}+\frac{\gamma}{2}\right)^2G(\phi_a,f)\right\}(1+c\tilde{\delta}) & \frac{\tilde{L}_r}{2}\le\tilde{\delta}\le\tilde{L}_c \end{cases}$$

where

$$\sigma_0=\frac{1}{2}V_f\tau_0(L_f/d_f),\quad c=\frac{\beta L_f}{2d_f}$$

$$\gamma=\sqrt{8G_d/(\tau_0\delta_0^*)},\quad \delta_0^*=\frac{\tau_0L_f^2}{E_fd_f(1+\eta)},\quad \delta^*=\delta_0^*(1+\gamma),\quad \tilde{\delta}^*=\delta^*/(L_f/2)$$

$$\tilde{L}_{c0}=\frac{\sigma_{fu}d_f}{2\tau_0L_f},\quad \tilde{L}_c=L_c/(L_f/2)=\tilde{L}_{c0}-\frac{\gamma}{2},\quad \tilde{L}_r=L_r/(L_f/2)=2\tilde{L}_{c0}e^{-(f+f')\pi/2}-\gamma$$

$$\tilde{\delta}_u(\phi)=\frac{L_{c0}^2}{(1+\gamma)}\tilde{\delta}^*\left[e^{-2(f+f')\phi}-\left(\frac{\gamma}{2\tilde{L}_{c0}}\right)^2\right]$$

$$\phi_c=-\frac{1}{2(f+f')}\ln\left(\frac{\tilde{\delta}}{\tilde{\delta}_{c0}}+\frac{\gamma^2}{4\tilde{L}_{c0}^2}\right),\quad \tilde{\delta}_{c0}=\tilde{L}_{c0}^2\tilde{\delta}^*/(1+\gamma)$$

$$\phi_b=-\frac{1}{(f+f')}\ln\left(\frac{1}{\tilde{L}_{c0}}+\frac{\gamma}{2\tilde{L}_{c0}}\right)$$

$$\phi_a=-\frac{1}{(f+f')}\ln\left(\frac{\tilde{\delta}}{\tilde{L}_{c0}}+\frac{\gamma}{2\tilde{L}_{c0}}\right)$$

For 3-D distribution:

$$G(\phi,f)=\frac{1}{4+f^2}\left[e^{f\phi}(f\sin2\phi-2\cos2\phi)+2\right]$$

$$g=G(\pi/2,f)$$

$$A(\phi,f)=\frac{1}{4+f^2}\left[e^{f\phi}(2\cos2\phi-f\sin2\phi)+2e^{f\pi/2}\right]$$

$$B(\phi_1,\phi_2,f)=\frac{1}{4+f^2}\begin{bmatrix}e^{f\phi_2}(f\sin2\phi_2-2\cos2\phi_2)\\-e^{f\phi_1}(f\sin2\phi_1-2\cos2\phi_1)\end{bmatrix}$$

For 2-D distribution:

$$G(\phi,f)=\frac{4}{\pi(1+f^2)}\left[e^{f\phi}(f\cos\phi+\sin\phi)-f\right]$$

$$g=G(\pi/2,f)$$

$$A(\phi,f)=\frac{4}{\pi(1+f^2)}\left[e^{f\pi/2}-e^{f\phi}(f\cos\phi+\sin\phi)\right]$$

$$B(\phi_1,\phi_2,f)=\frac{4}{\pi(1+f^2)}\begin{bmatrix}e^{f\phi_2}(f\cos\phi_2+\sin\phi_2)\\-e^{f\phi_1}(f\cos\phi_1+\sin\phi_1)\end{bmatrix}$$